

Journal of Geophysical Research: Solid Earth

RESEARCH ARTICLE

10.1002/2017JB013975

Key Points:

- High-frequency P and S wave reflections extracted using station autocorrelations
- Improved processing allows access to shallow reflections
- Successful application to ice and bedrock situations

Supporting Information:

- Supporting Information S1

Correspondence to:T.-S. Pham,
thanhson.pham@anu.edu.au**Citation:**

Pham, T.-S., and H. Tkalcic (2017), On the feasibility and use of teleseismic P wave coda autocorrelation for mapping shallow seismic discontinuities, *J. Geophys. Res. Solid Earth*, 122, doi:10.1002/2017JB013975.

Received 12 JAN 2017

Accepted 13 APR 2017

Accepted article online 20 APR 2017

On the feasibility and use of teleseismic P wave coda autocorrelation for mapping shallow seismic discontinuities

Thanh-Son Pham¹  and Hrvoje Tkalcic¹ ¹Research School of Earth Sciences, Australian National University, Canberra, ACT, Australia

Abstract Seismic body waves from distant earthquakes, which propagate near vertically beneath recording stations, provide tools for imaging shallow Earth structures with high vertical resolution. The most commonly used techniques such as P and S wave receiver functions utilize mode conversions from P to S waves or vice versa to retrieve information on the gradients of elastic properties in the crust and upper mantle. Here we demonstrate the feasibility and advantage of utilizing reflection signals through an improved method of teleseismic P wave coda autocorrelation. We recover clear reflections independently on vertical and radial components, which provide complementary constraints on the subsurface structures. Field data from two stations from different geological settings are analyzed, one of which is an ice station in Antarctica and the other is a bedrock station on the Kaapvaal craton in South Africa. The results from both analyses show the feasibility of the method to unveil P and S wave reflection signals from the ice-rock interface and the Moho discontinuity. Extensive synthetic experiments are set up to corroborate our results.

1. Introduction

Seismic waves from distant earthquakes arriving at seismic stations propagate near vertically and reflect from the free surface, propagate downward, and, subsequently, reflect back to the surface. Thus, a single station can be used to convert a coda wave train to a reflectivity record by means of computing the autocorrelation. The theory behind this idea was first proposed by *Claerbout* [1968] for the case of acoustic waves at vertical incidence on a horizontally stratified media and subsequently expanded to the case of elastic waves for inclined propagation by *Frasier* [1970].

The exploitation of the autocorrelation of records at a single station has recently emerged as a powerful imaging tool for mapping crustal and upper mantle structures. Most studies have used stacked autocorrelation of ambient noise to extract P wave reflectivity records to determine the Moho discontinuity [e.g., *Tibuleac and von Seggern*, 2012; *Gorbatov et al.*, 2013; *Kennett et al.*, 2015; *Taylor et al.*, 2016; *Oren and Nowack*, 2017] or the lithosphere-asthenosphere boundary [e.g., *Kennett*, 2015]. The recent study by *Oren and Nowack* [2017] introduced several processing steps to improve the ambient noise autocorrelation technique for selected USAArray Earthscope Transportable Array stations. Our study promotes the use of earthquake signals having well defined incident angles [e.g., *Ruigrok and Wapenaar*, 2012; *Sun and Kennett*, 2016]. By concentrating on the coda of a seismic phase, such as the first P arrival, the incoming energy can be confined to near-vertical incidence by selecting sources in an appropriate epicentral distance range. This selection is fundamentally different from the approach utilizing ambient noise and requires a much smaller amount of quality-controlled data and computational effort to produce a comparable reflectivity record [e.g., *Lin and Tsai*, 2013]. Because ambient noise energy is diffuse and has no specific directions, a large amount of data (months to years) has to be employed with stacking to yield destructive interference of horizontal energy and constructive interference of vertically reflecting energy.

In this study, we demonstrate the feasibility of exploiting the autocorrelation of the coda of the first P arrival from distant earthquakes (having epicentral distance larger than 30°). At those epicentral distances, the wavefront arriving at the recorder can be approximated by a plane wave with a steep angle of incidence that illuminates local structure from below. We confine ourselves to the P wave coda, which is the first arrival in the seismic wave train and thus is free of contamination by the coda of other phases [e.g., *Rondenay*, 2009]. In principle, other primary phases (e.g., S and PP) can be alternatively used with appropriate epicentral distance to the events.

The choice of input data is similar to that used with the conventional P wave receiver function technique [e.g., *Vinnik*, 1977; *Langston*, 1979]. A receiver function is generated by deconvolving radial by vertical components

of the P wave coda, in order to isolate the local structure effect from the complexities of the source time function and the raypath effect between the source and the receiver. Receiver functions can be exploited to extract the signal of P to S conversions at seismic interfaces below the stations. On the other hand, our autocorrelation approach exploits the time repetitions in the coda waveform recurrences to reveal and isolate reflection signals from subsurface reflectors.

In principle, both methods can be used to invert for a 1-D local seismic profile or to produce 2-D or 3-D images of the local media with an imaging principle such as the common conversion point stacking for receiver functions, or more generally, migration [e.g., *Rondenay*, 2009]. Horizontal component records containing converted energy can also be used in conjunction with the autocorrelation technique [e.g., *Tibileac and von Seggern*, 2012; *Sun and Kennett*, 2016]. The use of radial components promises to provide independent information on the local structure from both P and S waves.

In the next section, we focus on the practical interpretation of P wave coda autocorrelogram. We present some innovations in data processing to deal with the source contributions. In the subsequent section, we set up a scheme of synthetic experiments to guide the interpretation of results and then demonstrate the method with data from two stations having their most prominent reflectors at different scales. The first receiver is deployed over ice where the most prominent reflector is the ice-rock interface. The second example reveals reflection signals from an exceptionally sharp Moho discontinuity.

2. A Practical Interpretation of P Wave Coda Autocorrelogram

To facilitate the interpretation of P wave coda autocorrelograms, we consider the simple configuration sketched in Figure 1a with a homogeneous layer over a half space with different properties. A receiver at the surface records an impulsive compressional plane wave arriving near vertically. In horizontally stratified media, $P\text{-}SV$ waves are decoupled from the SH component; thus, vertical and radial components entirely account for the ground motion of the initial P wave arrival (Figure 1b). The transmitted ray P (1p—refer to the caption of Figure 1 for ray naming convention) arrives first on the seismogram, and the following pulses are the conversion P to S (1s) at the subsurface discontinuity, and multiple reflections of transmitted P or converted S wave within the layer.

By cross correlating an impulsive seismogram with itself (autocorrelating), any pair of original pulses collapse into a single pulse and its mirror reflection at time zero. Due to this symmetry, we consider only the causal (positive offset), one-sided autocorrelogram in our method. The large-amplitude central pulse, which is an inherent feature of any autocorrelogram, is suppressed by a taper function. Then, the most prominent pulse in the vertical one-sided autocorrelogram (Figure 1c), indicated as $2p$, is formed by the cumulative contributions of all pairs having the same time difference with the transmitted phase 1p and the reflection 3p:

$$\Delta t_{2p} = t_{3p} - t_{1p} = 2H\sqrt{\frac{1}{V_p^2} - \beta^2} = 2H\eta_p \quad (1)$$

where H is the layer thickness, V_p is the P wave velocity, β is the ray parameter of the plane wave, and η_p is the P wave vertical slowness [e.g., *Zhu and Kanamori*, 2000]. We also refer to the phase as a P wave single reflection, meaning a down reflection at the free surface and an up reflection from the interface. Each P wave leg takes the time of $H\eta_p$ to transverse a vertical cross section of the layer. Moreover, the phase has a negative polarity because one of its contributors experiences a phase flip due to free surface reflection while the other does not.

Likewise, other reflection phases in Figure 1c can also be formed in a similar fashion. For example, the S wave single reflection $2s$ in the radial autocorrelogram is contributed by all phase pairs having the same time difference with the $1p$ and $1p2s$ couple. The $2s$ delay time is also given by equation (1) with V_p replaced by shear wave velocity V_s , or $2H\eta_s$. The $s\text{-}p$ phase is similar to the converted Ps phase in the receiver function and is mainly contributed by the $1p$ and $1s$ pair and has a delay time of $H(\eta_s - \eta_p)$. Also, the $1p$ and $2p1s$ pair interacts to form the $p + s$ phase which has a delay time of $H(\eta_p + \eta_s)$.

Moreover, Figure 1c illustrates a fundamental difference between the P wave receiver function and the autocorrelation technique. The receiver function favors the mode-conversions ($s\text{-}p$ and $p + s$ phases), while the autocorrelation emphasizes the reflection phases ($2p$ and $2s$). The phase $2p$ is unique to the vertical

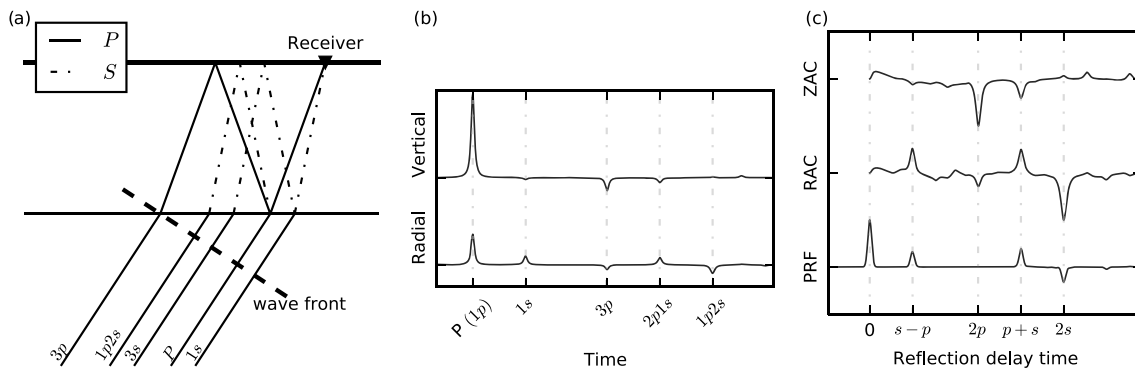


Figure 1. (a) Schematic representation of a plane wave (thick dashed line) approaching a receiver and its first-order reverberations for a homogeneous layer above a half space (P and S wave legs are solid and dashed-dotted lines, respectively). We follow Niu and James [2002] to use the notation n pm s for a ray having n P wave and m S wave legs within the layer. This naming scheme focuses on the observed delay time not the specific ordered combination of legs in its raypath. (b) Vertical and radial components of the structure impulse response. (c) Comparison of (from top to bottom) one-sided vertical autocorrelogram (ZAC), which is obtained by cross correlating the vertical impulse response with itself; and one-sided horizontal autocorrelogram (RAC); and P wave receiver function (PRF), which is obtained by deconvolving the radial by vertical component. These autocorrelograms are tapered to suppress the characteristic central peak at time 0. Reflection phases are named after their delay time (refer to the section 2 in the main text).

autocorrelation and thus does not occur in the receiver function. The autocorrelation approach promises to provide new information on P wave structure of the shallow Earth's interior that is different from S wave structure recovered by receiver function. Hence, the autocorrelation of P wave coda can be used in conjunction with the receiver function technique in order to increase constraints on the crust.

The seismic wavefield from a distant event is initiated by a source and subsequently modulated and attenuated along its raypath before interacting with the local structure and finally being recorded at a receiver on the surface. Due to attenuation in the Earth interior, most high-frequency signals dissipate along the path. Hence, the recorded waveform is a temporal convolution of the local structure response with source and path effect whose frequency content is biased toward the lower end of the spectrum. The autocorrelation of the recorded waveform convolves the source and raypath autocorrelation with the autocorrelation of the impulse response of the local structure. Consequently, the autocorrelation of the seismogram is much more complicated than our simple impulsive illustrations. The influence of the source and path effects represents a fundamental challenge for autocorrelation applications in high-resolution seismic imaging. In previous studies using earthquake signals, Ruigrok and Wapenaar [2012] exploited array stacking to suppress the common term in individual station autocorrelograms, while Sun and Kennett [2016] addressed the challenge with a high-frequency band-pass filter (i.e., 0.5–4 Hz). Here we attempt to address the issue by homogenizing the contribution of frequency components in an appropriate band.

3. Method

3.1. Data Selection and Preprocessing

We extract P wave coda of events with $M_w \geq 5.5$ and epicentral distance larger than 30° from stations in the global centroid moment tensor catalog (GCMT) [Ekström *et al.*, 2012]. Earthquakes in the distance range $95\text{--}120^\circ$ are automatically rejected to avoid the complication of P wave diffraction at the core-mantle boundary. The remaining events are separated into two data sets. The teleseismic data set includes events in the epicentral distance range $30\text{--}95^\circ$, and the global teleseismic data set includes events beyond 120° , which have raypaths sensitive to the Earth's core. The former data set has been used commonly in receiver function studies [e.g., Tkalcic *et al.*, 2011], because, in that epicentral distance range, P wave incident angles favor efficient energy conversion to S waves at discontinuities within the crust and upper mantle, e.g., the Moho.

Seismograms from the selected events are manually inspected and preprocessed for quality control purposes. Visual inspection identifies seismograms that contain a clear P onset with a good signal-to-noise ratio and is uncontaminated by subsequent primary phases such as the source-side surface reflection pP . Consequently, vertical seismograms, typically characterized by higher signal-to-noise ratio onsets, are more often selected than radial ones. In the following step, we select a window around the first P onset. The

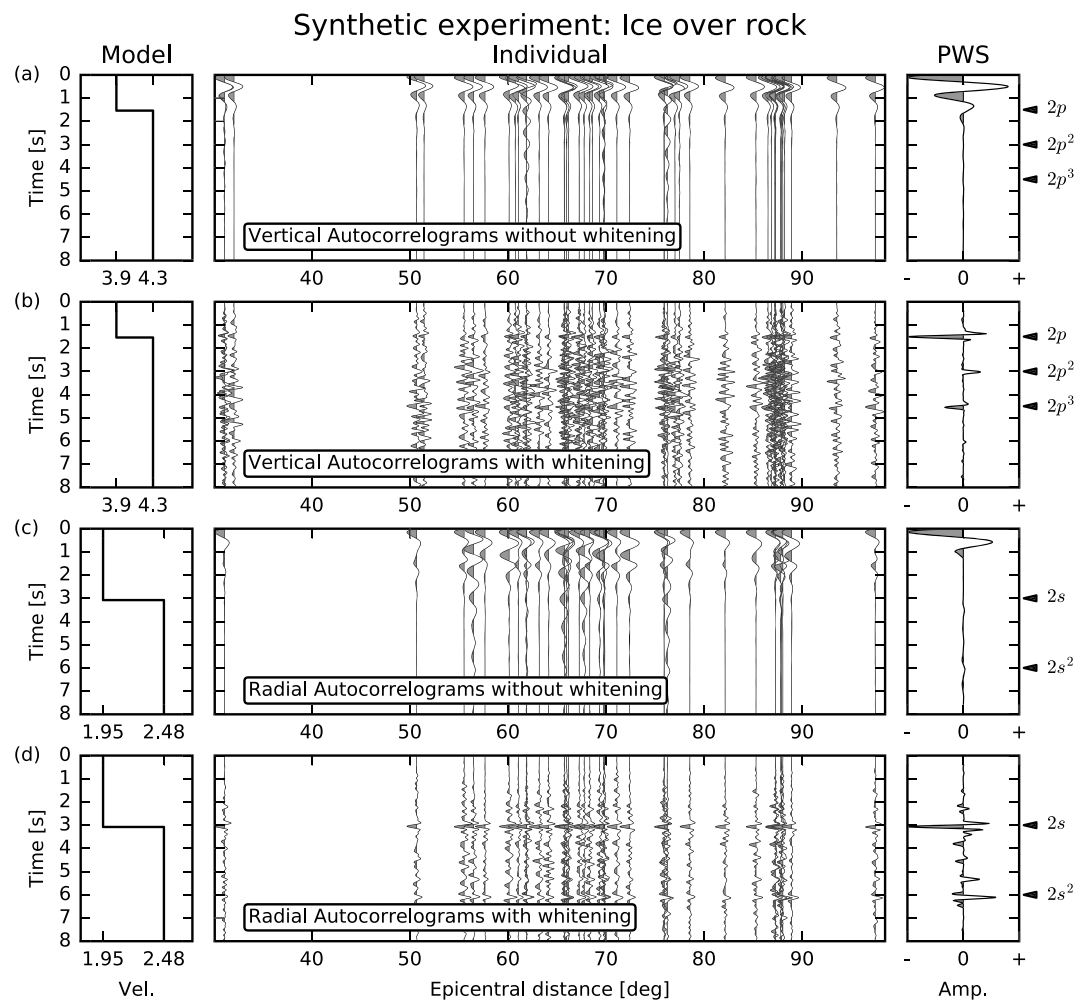


Figure 2. Synthetic experiment demonstrating the recovery of the ice-rock interface for a homogeneous ice layer over bedrock half space [Wittlinger and Farra, 2012, model 1, Figure 12]. The left column shows the input 1-D velocity profile of (a and b) P or (c and d) S waves, from which the discontinuity depths are converted to the vertical two-way reflection times of the corresponding waves. The middle column displays the one-sided autocorrelograms of individual seismograms as a function of their epicentral distances. The right column shows the stacked autocorrelograms. See section 2 for the naming convention of the reflection phases. The phases are marked at times predicted by ideally vertical incidence of both P and S waves. Vertical autocorrelograms without spectral whitening (Figure 2a). Vertical autocorrelograms with spectral whitening (Figure 2b). Radial autocorrelograms without spectral whitening (Figure 2c). Radial autocorrelograms with spectral whitening (Figure 2d).

window length is a generic parameter adapted to a particular type of application. In general, deeper discontinuities need longer seismograms to be resolved in the reflectivity records. Our examples in sections 5 and 6 use records of 30 s, starting at 5 s before the P onset, for the ice-rock interface (illustrative examples of the coda windows in use are in Figures 4 and 5) and 60 s, starting at 10 s before the P onset for application to the Moho. Lastly, we remove the linear trend and the mean from the short seismogram segments and retain the original sampling rate of 40 samples per second (or Nyquist frequency of 20 Hz) after multiple tests with different values.

We do not need to make any instrument correction in our applications. The autocorrelation retains the amplitude information of the response function but cancels the phase. Fortunately, in the frequency ranges considered in this study (i.e., 1.0–5.0 Hz for the ice-rock interface application and 0.25–1.0 Hz for the Moho discontinuity application), most broadband instruments have a response function with flat amplitude. Thus, the instrument response only serves as a scaling factor and does not perturb the autocorrelogram waveform [e.g., Gorbatov *et al.*, 2013].

3.2. Spectral Whitening

To address the problem of the bias toward lower frequencies in the records, we use an adaptive weighting function to normalize the complex spectrum of the original waveforms. Thus, we amplify the high-frequency content and reduce the low-frequency content at the same time. The spectral whitening (or balancing) operation is defined in a similar way to the running-absolute-mean normalization method in time domain [Bensen *et al.*, 2007], namely,

$$\hat{s}_n = \frac{s_n}{\frac{1}{2N+1} \sum_{j=n-N}^{n+N} |s_j|}, \quad (2)$$

where s_n is the complex spectrum of the original waveform and \hat{s}_n is its whitened complex spectrum. In the denominator, the amplitude spectrum $|s_n|$ is smoothed by an averaging filter to define the adaptive weighting function. The averaging window width ($2N + 1$) controls the local information of the power spectrum retained in the weighting function, which is inversely proportional to the global amplitude information preserved in the whitened spectrum. For example, when $N = 0$, the filtering window has only one element; thus, the local information of the power spectrum is conserved completely, but the whitened amplitude is destroyed and equals to 1 at all frequencies. In contrast, when N becomes very large, the weighting function is virtually constant for all entries, and the relative importance of each part of the spectrum does not change. For convenience, we use $\Delta W = 2N\Delta\omega$ (in Hz), where $\Delta\omega$ is the discrete frequency step of the complex spectrum, as an interchangeable measurement for the averaging window width.

In this study, we have not performed a comprehensive search for an optimal averaging window width ΔW . However, Figure S1 in the supporting information compares the performances of different window averaging widths applied to both field and synthetic data (find more details in section 6). In this study, we empirically use $\Delta W = 0.5$ Hz in the examples presented in sections 5 and 6 based on a visual comparison of the autocorrelation waveforms.

3.3. Computing Autocorrelation

We compute the autocorrelation of the whitened waveform in the frequency domain. The Fourier transform of an autocorrelation is real and equal to the power spectrum of its input waveform. In order to avoid aliasing effect, the length of the original trace is doubled with zero padding. Next, in the time domain, we retain a half of the symmetric autocorrelogram having positive time lags and use a cosine taper to suppress its characteristic zero-time peak. Then, we use a zero-phase band-pass filter to improve the sharpness of the reflection signal (by removing the very long period signals) and to avoid spurious effects caused by the unexpected amplification of very high frequency noise due to the spectral whitening. In section 5, we use a frequency band of 1.0–5.0 Hz for the ice-rock interface application and 0.25–1.0 Hz for the Moho discontinuity application in section 6. Subsequently, the filtered causal autocorrelograms are normalized by its maximum amplitude before stacking.

3.4. Phase-Weighted Stacking

We have elaborated on the principle of recovering and amplifying reflections induced by subsurface discontinuities from a single event seismogram. However, in practice, individual autocorrelograms are characterized by a significant amount of noise. Thus, we stack the autocorrelograms of many events repeatedly illuminating the structures at similar incident angles to obtain coherent reflection signals.

In this study, we use the phase-weighted stacking method (PWS) [Schimmel and Paulsen, 1997]. Given a number of N individual one-sided autocorrelograms $s_n(t)$, their analytical signals are defined as

$$S_n(t) = s_n(t) + i H_n(t) = A_n(t) e^{i\phi_n(t)} \quad (3)$$

where $H_n(t)$ is the Hilbert transform of the original trace $s_n(t)$, and $A_n(t)$, $\phi_n(t)$ are the amplitude and phase components. The amplitude of the analytical phase average, representing a measure of coherence among all signals in the stack, is used to weight their linear stack:

$$g(t) = \frac{1}{N} \sum_{n=1}^N s_n(t) \left| \frac{1}{N} \sum_{n=1}^N e^{i\phi_n(t)} \right|^{\eta}, \quad (4)$$

where $\eta \geq 0$ is the PWS order and $g(t)$ is the phase-weighted stack. The order of PWS, η , controls the contribution of the overall coherency measure in the final stack. If $\eta = 0$, PWS becomes linear stacking while, η is large, the coherency measure dominates the stack and makes it strongly distorted. We have found that the second-order PWS ($\eta = 2$) gives the best results. Figure S2 in the supporting information illustrates the advantage of PWS against linear stacking in suppressing noise.

4. Design of Synthetic Experiments

In this section, we describe the procedure we have adopted to conduct synthetic experiments for different geological settings. The synthetic tests illustrate the capacity of the P wave coda autocorrelation technique to isolate reflection responses from sharp and relatively shallow discontinuities. In particular, we wish to understand (i) which reflection phases can be practically recovered by P wave coda autocorrelation and what are their polarities and (ii) how the dependence of reflection delay times on ray parameter, as characterized by equation (1), influences the final stack.

The experiments are designed to synthesize (both vertical and radial) complete seismograms recorded for a receiver on top of a horizontally stratified media bounded by a free surface. Since the distance to the events is much larger than the extent of the local structure of interest, we simulate the teleseismic wavefronts as plane waves, which illuminate the local structure from below at different incident angles. There are two steps involved in the procedure. The first is to generate the temporal impulse response of the local structure to a plane wave arrival, and the second is to produce a randomized waveform that simulates the cumulative effect of source and traveling raypath being dominated by low-frequency content.

To generate the structure impulse response, we use the reflectivity code (respknt) of *Randall* [1989], who implements the reflection and transmission matrix methods developed by *Kennett* [1983]. The procedure is similar to *Tkalčić et al.* [2011], in which the program is used to synthesize receiver functions for 1-D Earth models. Epicentral distances are converted to ray parameters, which are used as inputs to control the incident direction of the incoming plane waves. We can thus simulate the distance distributions of the real earthquakes for the two data sets used in the subsequent sections.

Waveforms encompassing both the source and raypath effects are synthesized in a random manner to simulate P wave coda waveforms from different events used at a single station. First, we generate an array of normally distributed random numbers with mean 0 and standard deviation 1. The time duration is chosen uniformly between 8 and 12 s, which is approximately equivalent to a M_w 6.0 earthquake. This time series is then low-pass filtered by a third-order Butterworth filter to introduce low-frequency components and finally is tapered at both ends in the time domain. The corner frequency has a uniformly random distribution between 0 and 0.5 Hz. We find that the Butterworth filtering has a similar effect to the Earth attenuation because it does not sharply stop the signals beyond the frequency corner but gradually weakens their energy.

We convolve the structure impulse response with the randomly generated time series to produce a complete seismogram. This scheme is repeated for every epicentral distance for vertical and radial components, if applicable. An example of the components and a complete synthetic seismogram is given in Figure S3 in the supporting information.

5. Recovering Reflections From Ice-Rock Interface in Antarctica

The setting with ice over bedrock, which is common in Antarctica, presents an interesting case for applying the autocorrelation technique to map the ice-rock interface. According to *Kohnen* [1974], the P wave velocity of the Antarctic ice sheet varies slightly with temperature around 3.9 km/s, and the Poisson ratio is approximately 0.33 (equivalently $V_p/V_s \sim 2$). In general, the seismic properties are stable throughout the whole ice column, except for a couple of hundred meters of unconsolidated snow at the top (also known as the firn layer) where there is a gradient in both velocity and density [e.g., *Anandakrishnan and Winberry*, 2004; *Zhan et al.*, 2014]. Thus, for most seismological applications, the ice sheet can be reasonably approximated as a homogeneous layer, with significantly lower seismic wave speeds and density than the crustal rocks below. The sharp impedance contrast at the ice base reflects a remarkable

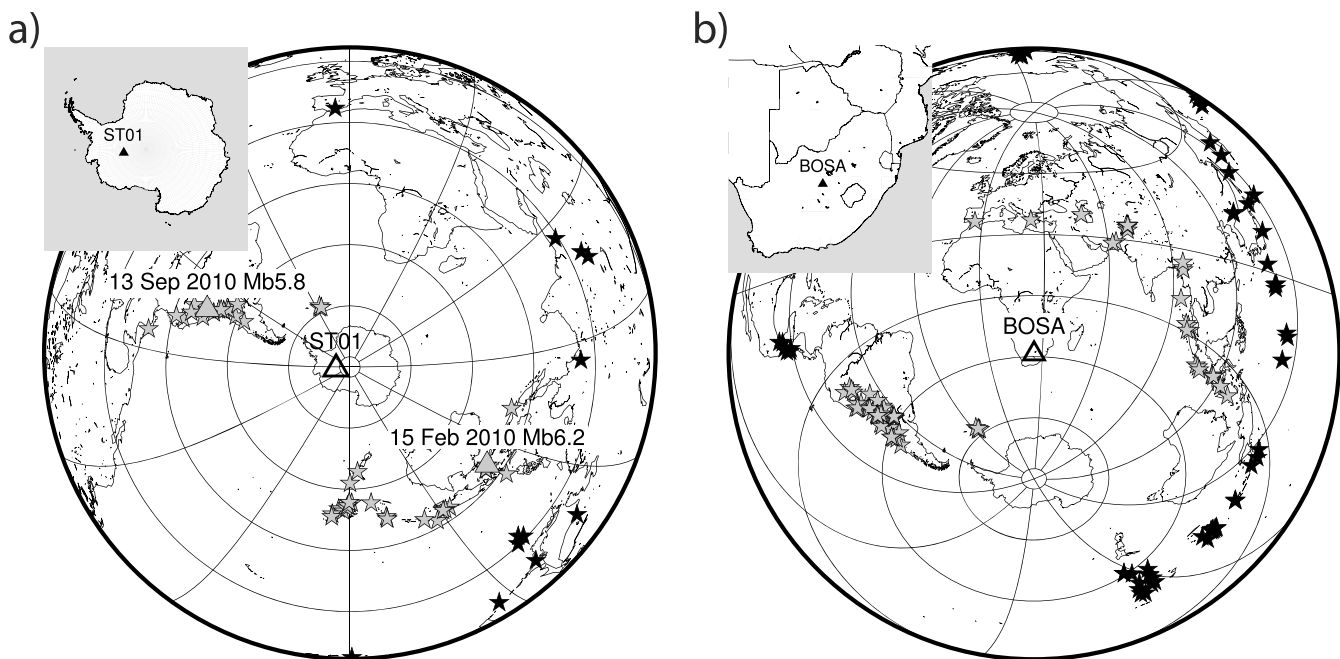


Figure 3. (a) Location of the temporary ice station ST01 (the Polar Observation Network) [Chaput et al., 2014] deployed in the West Antarctica Ice Sheet. The inset shows the station location at a greater detail. Stars denote the earthquakes contributing to the waveform data sets on this station. Gray and black events belong to the teleseismic data set (epicentral distance from 30° to 95°) and the global teleseismic data set (epicentral distance larger than 120°), respectively. The labeled gray triangles mark the events shown in Figures 4 and 5. (b) Same as in Figure 3a but for the permanent bedrock station BOSA in the Kaapvaal craton, South Africa.

amount of precritical downgoing energy from the surface back to the ice sheet. In one hand, the strong reverberations usually mask the conversion of energy at deeper discontinuities, e.g., the Moho. Thus, the widely used technique of P wave receiver function has limited use in studying Antarctic crustal structure, despite the fact that it gained significant success in some regions [e.g., Hansen et al., 2009, 2010; Ramirez et al., 2016]. On the other hand, the presence of a sharp discontinuity provides a favorable situation for the reflection-based autocorrelation techniques [e.g., Gorbatov et al., 2013; Kennett, 2015]. Because the method utilizes a single station, precritical reflections play a vital role in the recurrence of energy in seismic waveforms, which in turn is essential for the success of autocorrelation techniques.

At the same time, the relatively small thickness of the ice sheet also introduces challenges for the use of autocorrelation techniques. The thickness fluctuates around 2 km and up to 5 km [Fretwell et al., 2013], and so a considerable amount of energy concentrated in a high-frequency band is needed to resolve the ice base [Wittlinger and Farra, 2012]. The fundamental mode of reverberated waves presents a lower limit for the frequency band that is sensitive to the ice base. In the vertical direction, the ice sheet model can be simplified as an elastic band being bounded by a fixed end at bottom (due to a significant impedance difference between ice and basal bedrock) and a free moving end on top. The longest wavelength that satisfies the boundary condition is approximately 4 times larger than the ice thickness. For instance, for the case of P wave ($V_p \sim 4$ km/s) reverberating in an ice layer of ~ 3 km, the wavelength is ~ 12 km, and so the frequency threshold is ~ 0.33 Hz. However, the waveforms must contain far higher frequency content in order to resolve the ice base sharply (we will demonstrate this point with field data examples in section 5.2). This condition is not usually met when using seismograms of teleseismic earthquakes. Hence, to isolate the reflection signals in a teleseismic P wave coda, wave train is not a trivial task. The situation is somewhat similar in basin regions where a pronounced sediment layer is present on top of crustal bedrock.

5.1. Synthetic Experiment

A typical Earth model for a station on an ice cap consists of an ice layer on top, a layer of crustal bedrock in the middle, and a mantle half space below [e.g., Cho, 2011; Hansen et al., 2010; Ramirez et al., 2016]. In this synthetic experiment, we use the parameters from model 1 of Wittlinger and Farra [2012, Figure 12]. The model has an ice

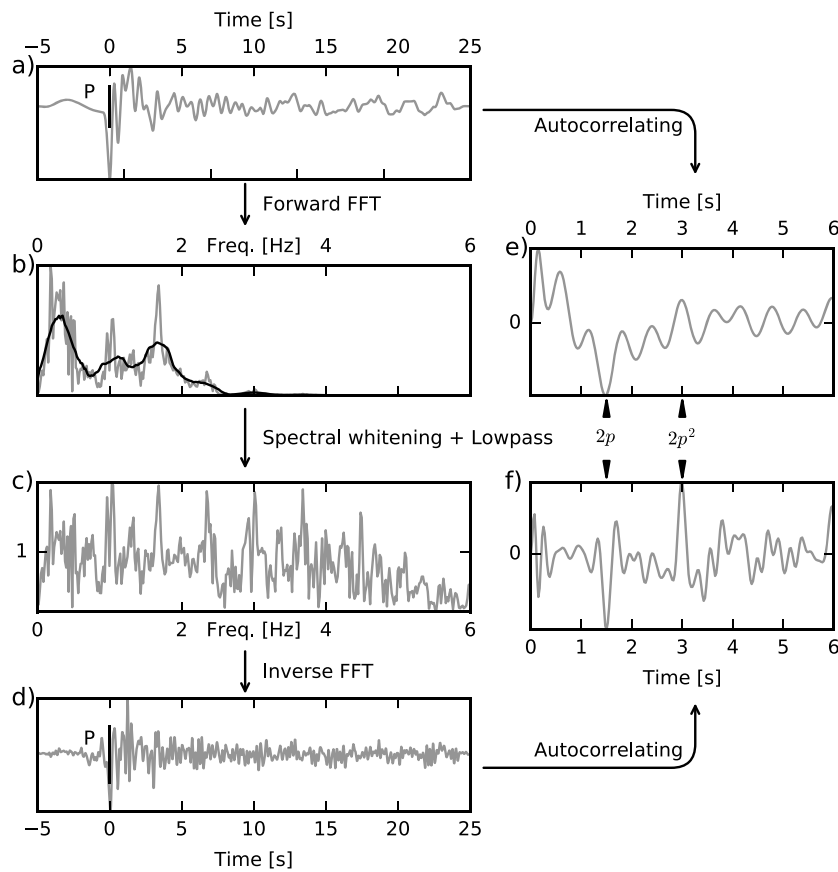


Figure 4. Data processing example for a single event. (a) Original vertical seismogram recorded at the ice station ST01 after the $M_b = 5.8$ event on 13 September 2010 (14.7°S, 71.1°W, 171 km depth). The location of this earthquake is specified in Figure 3a. (b) Original amplitude spectrum (gray line) and its smoothed average (black line). (c) Whitened amplitude spectrum obtained by dividing original complex spectrum by its smoothed trace shown in the previous column. The trapezoid shape enveloping the spectrum is due to the filter. (d) Spectrally whitened seismogram in time domain. (e) One-sided autocorrelogram of the original seismogram. (f) One-sided autocorrelogram of the whitened seismogram. The central peaks at time 0 are tapered by a cosine function.

layer of 3 km thickness, P wave velocity 3.90 km/s, S wave velocity 1.95 km/s, and density 0.92 g/cm³. These values are in good agreement with empirical measurements of the Antarctic ice cap [Kohnen, 1974].

Figure 2 shows synthetic autocorrelograms for the ice-over-bedrock model. To capture the shallow ice-bedrock interface, we only show the first 8 s of the one-sided autocorrelograms. There is a clear difference in the reflection patterns in autocorrelograms processed with spectral whitening or without (comparing Figures 2a and 2b and 2c and 2d). When spectral whitening is applied (Figures 2b and 2d), negative phases at around 1.5 and 3.0 s are visually coherent on most individual vertical and radial autocorrelograms. Consequently, they stack constructively into the most pronounced negative phases, which are at the expected time of the (transmitted) P and (converted) S wave single reflections ($2p$ and $2s$). Moreover, multiple reflections (e.g., $2p^2$, $2p^3$, and $2s^2$) are also visible on the stacked autocorrelograms, even though they do not appear in the noisy individual autocorrelograms. The multiple phases have periodic delay times and alternative polarities as expected.

The negative reflection phases in both the vertical and radial autocorrelograms (Figures 2b and 2d) have almost perfect horizontal alignment. Thus, to a good approximation, we can neglect the dependence of P and S wave reflection times on the seismic ray parameter by omitting the term of ray parameter β in equation (1), since both wave speeds V_p , V_s , and the thickness H are small for ice. This experiment shows that in the selected epicentral distance range (above 30°), the dependence on ray parameter does not affect the stack or the measurement of two-way reflection times from the ice base and so the delay times

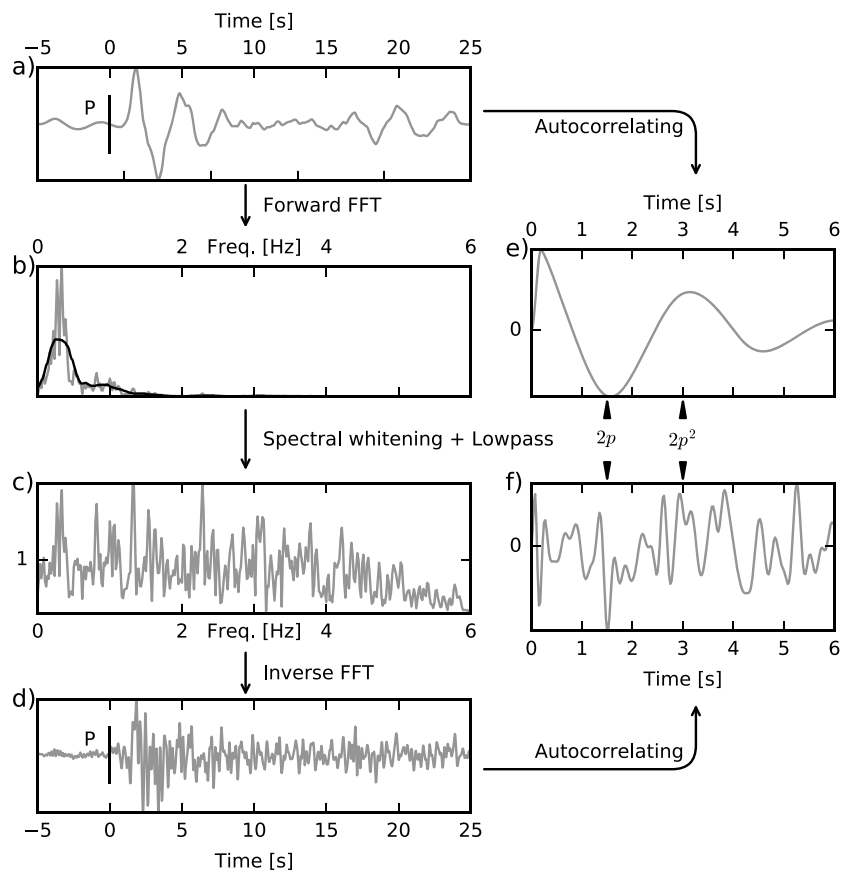


Figure 5. Same as Figure 4, but for the $M_b = 6.2$ event from 15 February 2010 (7.4°S, 128.7°E, 136 km depth) recorded at the ice station ST01. The location of this earthquake is specified in Figure 3a.

measured in the stacks are approximately the vertical two-way reflection times of corresponding waves. Consequently, because the reflection times can be obtained separately from the stacks, we can recover the gross V_p/V_s ratio of the ice layer by taking the ratio of their delay times.

5.2. Results for ST01

We use data from a pilot station ST01, situated on the West Antarctica Ice Sheet. The station operated from 2011 to 2012 in a temporary seismic network that belongs to a multidisciplinary research project named the Polar Earth Observation Network [Chaput *et al.*, 2014]. Figure 3a shows a map of the station and the earthquakes employed for its waveform data sets. Raw seismic data were downloaded from the IRIS Data Management Center (IRIS DMC). The selection procedure (section 3) results in 50 vertical and 36 radial seismograms in the teleseismic data set and 12 vertical seismograms in the global teleseismic data set (see section 3.1 for the definition of those data sets).

We first consider the autocorrelation of two individual vertical seismograms to provide insight into the application of our procedure. The ice thickness beneath station ST01 is around 3 km [e.g., Hansen *et al.*, 2010; Fretwell *et al.*, 2013], which is similar to the value set in the synthetic experiments. Therefore, the single-reflection signals of P and S waves are expected to arrive at two-way times of approximately 1.5 and 3.0 s, given the “standard” seismic velocities in ice (3.95 km/s and 2.00 km/s) [Wittlinger and Farra, 2012]. Figures 4 and 5 graphically summarize the processing steps applied for a single seismogram and compare their effects. Specifically, Figure 4 shows an example of an original seismogram having rich frequency content up to 2 Hz, which is far from the fundamental lower threshold of ~ 0.33 Hz. Consequently, the single and double P wave reflections appear clearly in its autocorrelation as expected. Moreover, when the whitening operation amplifies higher-frequency signals, the sharpness of those reflections improves significantly. In a second example, the frequency content of the original seismogram

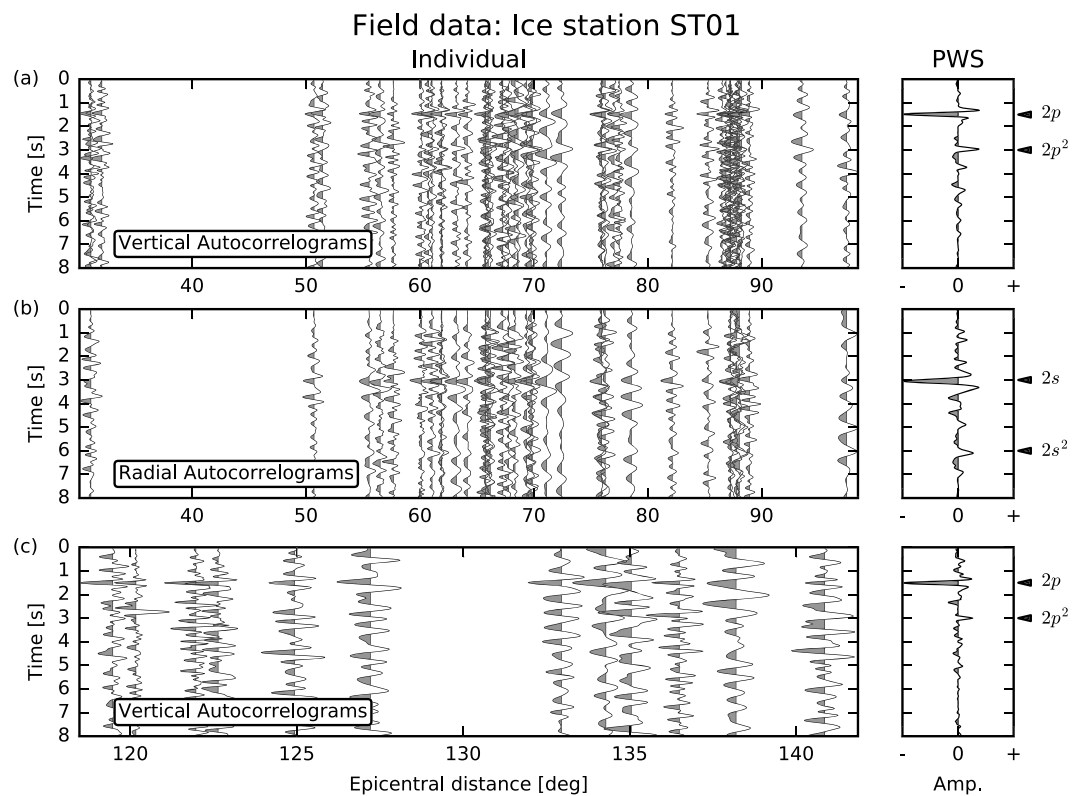


Figure 6. One-sided whitened autocorrelograms of field data recorded at ice station ST01, see Figure 3a for the geographical distribution of the events. (a) Vertical and (b) radial autocorrelograms of the P wave teleseismic data set; (c) and vertical autocorrelograms of the global teleseismic data set. For the explanation of the individual autocorrelograms (left panels) and stacked autocorrelograms (right panels), see the captions of Figure 2.

concentrates below 0.5 Hz (Figure 5). Therefore, its autocorrelogram modulates slowly and shows no clear signs of any reflected signal even though the autocorrelation waveform coincidentally has a trough close to the expected reflection time. The whitening plays a crucial role in this example since it unveils the buried reflection in the whitened autocorrelogram.

When we consider multiple events in Figures 6a and 6b, we get similar behavior on the influence of whitening as seen in the synthetic examples in Figure 2. There is a high level of similarity between both kinds of data. Both single and double reflections of P waves are clear on the vertical autocorrelogram stacks, with similar effects for S waves on the radial stacks. The delay times of reflection signals confirm the thickness of the ice sheet (~ 3 km) and the empirical ratio of V_p and V_s velocities (~ 2). Moreover, in Figure 6c, we repeat the analysis for the global teleseismic data set (events at epicentral distances above 120°). The resulting stack is a comparable reflectivity record although many fewer events are involved.

The above examples demonstrate clearly the feasibility of recovering signals from a shallow reflector recurring in the P wave coda wave trains.

5.3. Discussion

We have shown high-level agreement in reflection pattern for both synthetic and real data for the ice-over-bedrock case given the assumption of a homogeneous ice layer. However, this assumption has been scrutinized by previous workers. For example, Wittlinger and Farra [2012] claim evidence for inner ice stratification due to the change of anisotropy under pressure by the P wave receiver function technique at high frequency and a grid search stacking technique. At several stations, they report that while the compressional velocity remains almost constant, there is a decrease of $\sim 20\%$ in the near-vertical shear wave speed at the bottom-most third of the layer from the standard 1.95 km/s to ~ 1.6 km/s. Here we use synthetic experiments to test the ability to detect inner-ice structure.

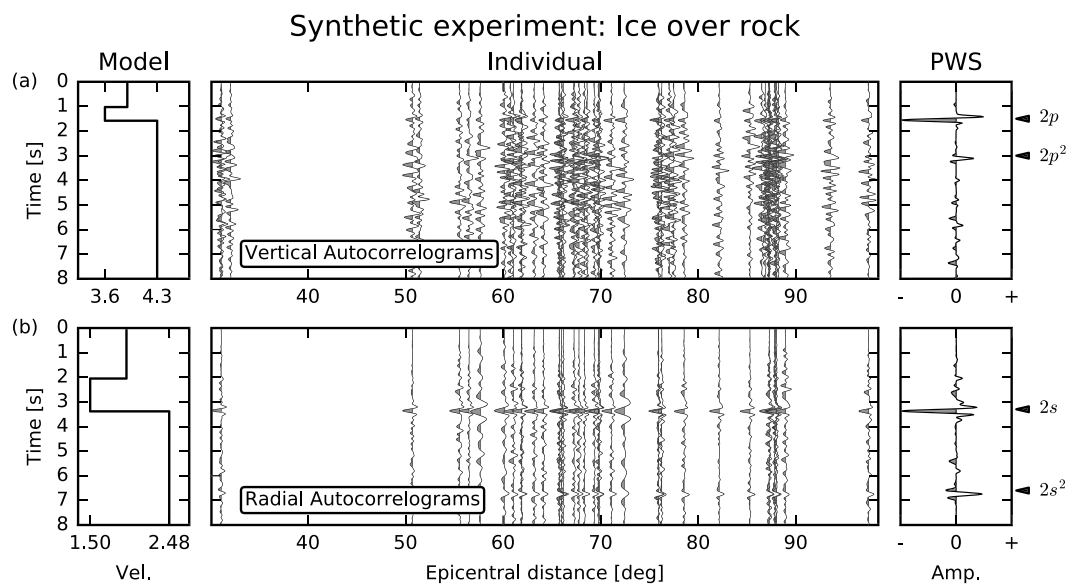


Figure 7. Synthetic test in detecting the inner-ice reflection for the stratified ice layer model [Wittlinger and Farra, 2012, model 2, Figure 12]. Both vertical and radial autocorrelograms are whitened. For the explanation of individual panels, see Figure 2.

In our experiments, we use parameters from Model 2 of Wittlinger and Farra [2012, Figure 12]. The synthetic reflection results of the stratified ice layer model are shown in Figure 7. Visually, the reflection patterns are highly similar between this model and the homogeneous ice model presented in Figure 2, although the S wave reflection is shifted downward. The observation means that our resolving power is not sufficient to detect the inner stratification, but we are able to see the change in the average V_s wave speed via the delayed S wave reflections.

The preservation of the reflection patterns is due to small shear wave impedance contrast (product of density and velocity) at the inner interface in comparison with the ice-bedrock interface. Indeed, although the reduction of the shear wave between ice layers is significant, its corresponding impedance contrast is much smaller than at the ice base because of small ice density ($\sim 0.9 \text{ g/cm}^3$ versus $\sim 2.7 \text{ g/cm}^3$ in bedrock). This example underscores the dominating effect of impedance in comparison with velocity contrast in the autocorrelation studies.

6. Recovering Reflections From a Sharp Moho Discontinuity in South Africa

The Kaapvaal craton, South Africa, has a widely known diamondiferous region; thus, many efforts to study its crustal structure have been conducted. Niu and James [2002] and James *et al.* [2003] present evidence for an exceptionally sharp and flat Moho discontinuity in a broad area beneath the craton. They use receiver function studies conducted at the Kimberley array that covers an area of $\sim 1000 \text{ km}^2$, to show that the Moho transition zone thickness is less than 0.5 km and the corresponding depth variation is less than 1 km. This craton has been used as a laboratory site for passive reflection studies. For instance, Zhan *et al.* [2010] demonstrated in a pioneering work the existence of the body wave components of Green functions recovered by ambient noise cross correlation. The cross correlograms between many station pairs show clear shear wave postcritical reflections at the Moho (SmS) and even their double multiples.

6.1. Synthetic Experiment

We use the 1-D crustal model of the Kaapvaal craton developed by James *et al.* [2003] for our synthetic tests. The model provides the best fit to the empirical receiver function obtained by stacking individual receiver functions of the Kimberley array's elements from the Welkom mine, $m_b = 5.7$ event that occurred on 22 April 1999. Since the array elements closely surround the permanent station BOSA, the model should reasonably represent the crust and upper mantle structures beneath the station. The profile features a gradual increase in both P and S waves and density from the surface down to the Moho discontinuity at $\sim 35 \text{ km}$,

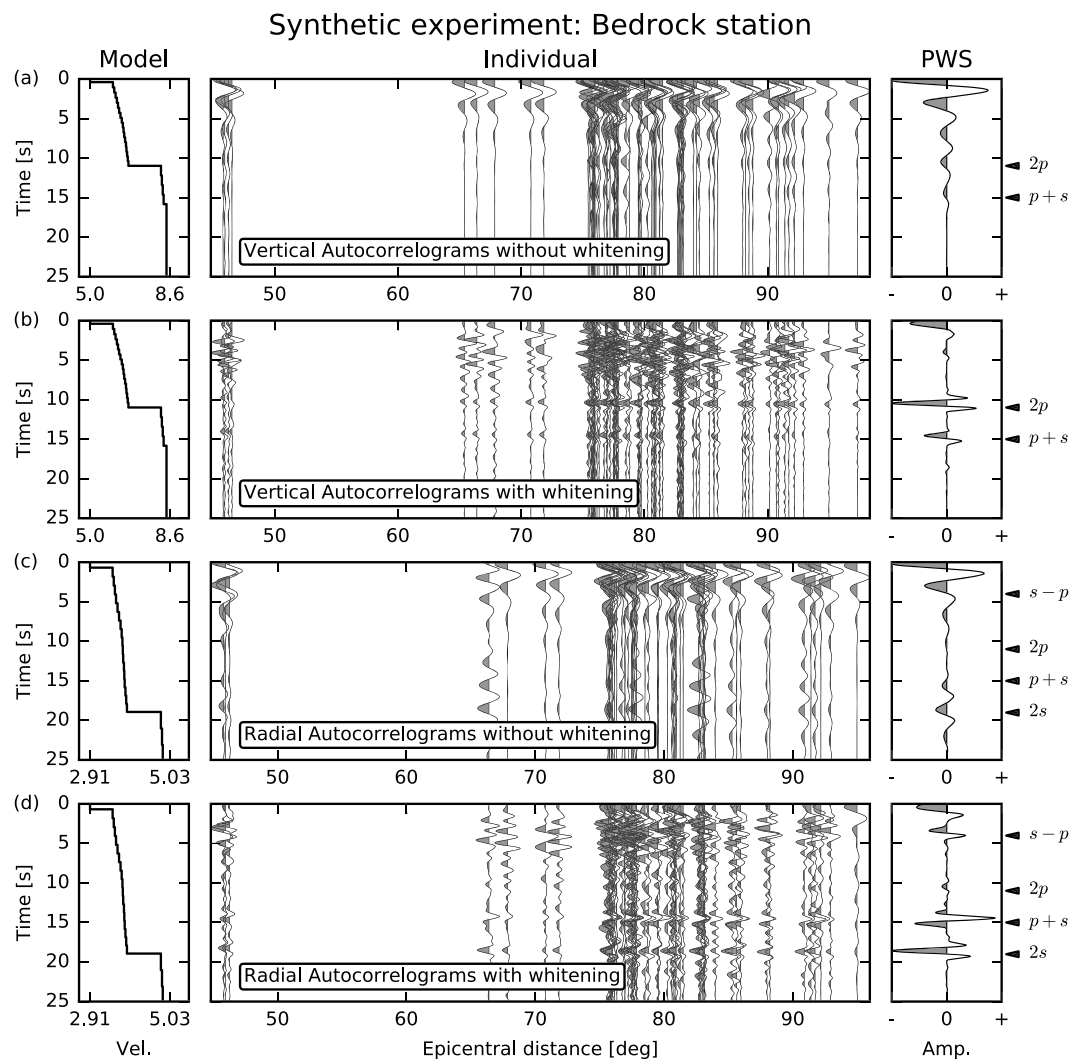


Figure 8. Synthetic experiment demonstrating the recovery of autocorrelation features associated with the Moho as in the Kaapvaal craton crustal model [James *et al.*, 2003], shown in the left column. For the explanation of the (middle column) individual autocorrelograms and the (right column) stacks, see Figure 2.

where a sudden jump of all parameters occurs (Figure 8, left column). The jump represents the most prominent reflectors in the model. The average P and S wave velocities within the crust are 6.37 km/s and 3.70 km/s.

The most conspicuous feature in the whitened autocorrelograms (Figures 8b and 8d) for the synthetic experiment is the coherence of negative phases close to the anticipated two-way reflection times of P and S waves ($2p$ and $2s$) in the vertical and radial autocorrelograms, respectively. Additionally, in the vertical autocorrelograms, a secondary converted phase $p + s$ also clearly appears, and it is even clearer in the radial autocorrelograms, which have a similar shape to classical receiver functions (Figure 1c). Beside the S wave single reflection, there are clear $s-p$ and $p + s$ phases, and a weak $2p$ phase in the radial autocorrelogram. The polarities of the phases are well defined in both individual autocorrelograms as well as in the stack.

The significant thickness of the crust (H) enlarges the dependence of reflection delay times on ray parameter in equation (1). Specifically, for a smaller epicentral distance, the wave plane arrives at a larger angle of incidence from the vertical or a larger ray parameter. Thus, delay times of the P and S wave reflections show a clear decreasing trend in individual whitened autocorrelograms (Figures 8b and 8d) toward closer epicentral distances. Consequently, there is a slight shift upward of reflection signals in the final stacks in comparison with the expected two-way reflection time of the absolute vertical direction (shown in the left column of

the model). In Figure 9, we make a correction for the slowness dependence using equation (1) for the phases. In practice, for the autocorrelogram of each event, we convert its epicentral distance to ray parameter, then to the incident angle using the average P and S wave velocities of the model, given that the crust is approximated as a layer. With this single-layer treatment, the time steps of the autocorrelation trace are expanded by dividing by the cosine of the incident angle; then the traces are resampled to the original sampling rate before being stacked. In Figure 9, both the P and S wave single reflections now align to the expected reflection times. However, as a side effect, since the correction is designed for the reflection phases $2p$ and $2s$, the other peaks are slightly shifted.

6.2. Results for BOSA

Station BOSA has been deployed on the Kaapvaal craton since 1993 and belongs to the Global Seismological Network providing high-quality seismic data. We have downloaded data from the IRIS DMC for the period 2010–2015. We have looked for a moment magnitude threshold of $M_w = 5.5$ from the GCMT catalog. The data selection results in around 80 vertical and 60 radial seismograms in the P wave teleseismic data set and 65 vertical seismograms in the global teleseismic data set. Figure 3b shows a map of the station and the selected earthquakes.

We show the autocorrelograms and stacks of seismic records from the teleseismic data set of station BOSA in Figures 10a and 10b. The correction for ray parameter dependence is made in the same way as for the synthetics. Apparently, reflection patterns of the stacks show a high level of similarity to the synthetic tests (Figure 9), even though the individual autocorrelograms are much noisier in the field data. After correction, the P wave single reflection in the vertically stacked autocorrelograms of both synthetic and real data agree at ~ 11 s (Figures 9a and 10a). On the radial components, the presence of other phases ($s-p$, $p+s$, and $2s$) is similar to the P wave receiver function computed for this station [James et al., 2003]. Moreover, their delay times are also well predicted with the P wave reflection time and the V_p/V_s ratio of 1.73. Thus, our reflection results reinforce the existence of the Moho at ~ 35 km as the most prominent reflector given that the average P wave velocity is 6.37 km/s.

Moreover, the vertical reflectivity records from the global teleseismic data set are displayed in Figure 10c. The incident angles of the core-sensitive P wave planes from the events in this epicentral distance range are small enough so that the epicentral corrections are not necessary. The small incident angles also explain the absence of the $p+s$ phase, which involves the converted S waves of inclined incidence. In the stack, the appearance of the P wave single reflection is prominent and its delay time shows good agreement with the teleseismic case shown in Figure 10a.

6.3. Discussion

In Figure 8, we compare the stacked synthetic autocorrelograms with and without applying the spectral whitening. We note that the reflected phases are much more prominent with whitening, even though they are present in both cases. Thus, even for a recovery of the Moho depth, the whitening step is important, because it helps reveal the reflections in almost all individual autocorrelograms, hence in the final stack. In contrast, only few raw (without whitening) autocorrelograms generated from seismograms with favorable frequency content have the reflection signals that contribute to the stack. In practice when noise levels are high, the noncontributing elements can significantly diminish the signals.

In both field and synthetic data, the existence of main reflection phases that can be recovered by autocorrelation is unquestionable. Though one can infer the existence and obtain the depth of the discontinuity from the delay times, the involvement of nonlinear operations such as the spectral whitening or phase-weighted stacking prohibits the use of the full waveforms to further inverse for the structure. The reason is that the operations are highly sensitive to high noise levels and so distort the shape and amplitude of the final waveforms.

A possible concern is related to the source-side arrivals of depth phases following the initial P onset, which potentially encapsulates information of prominent reflectors near the hypocenter and might cause ambiguities in the interpretation of the discontinuities beneath the receiver. Though we roughly prevent this possibility by rejecting coda waveforms with a visually recognizable surface reflection pP , hidden signals can still elude our visual inspection and then be amplified by the whitening in the same way the receiver-side signals do. However, the delay and polarity of the source-side signals, if they exist, must vary as not only a function of

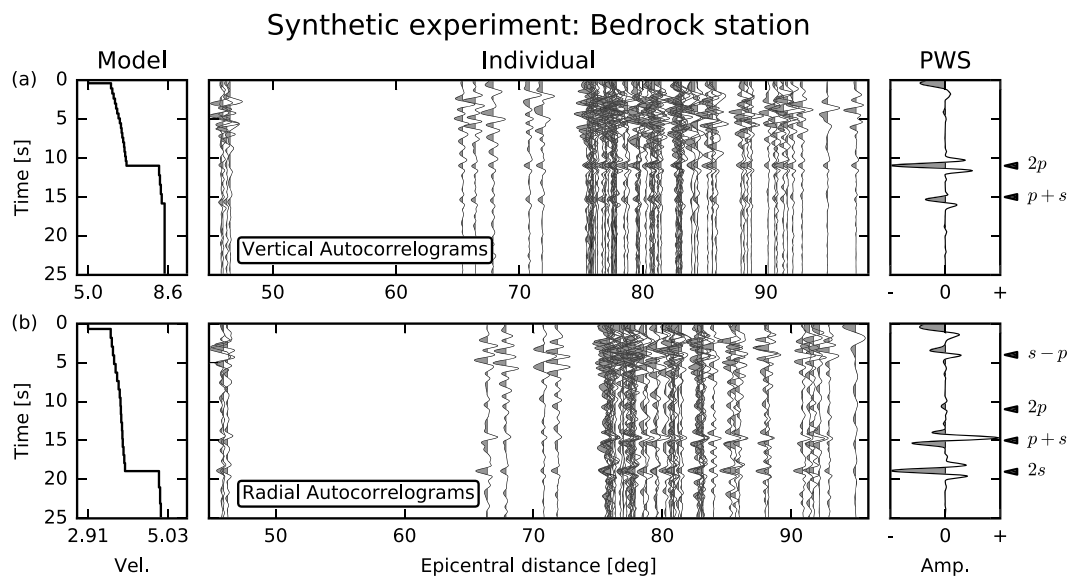


Figure 9. Synthetic experiment demonstrating the recovery of the autocorrelation features associated with the Moho depth as in the Kaapvaal craton crustal model [James et al., 2003]. Both vertical and radial autocorrelograms are whitened. The autocorrelograms are similar to those shown in Figures 8b and 8d, but they are corrected for the dependence on ray parameters. For the explanation of individual column, see Figure 2.

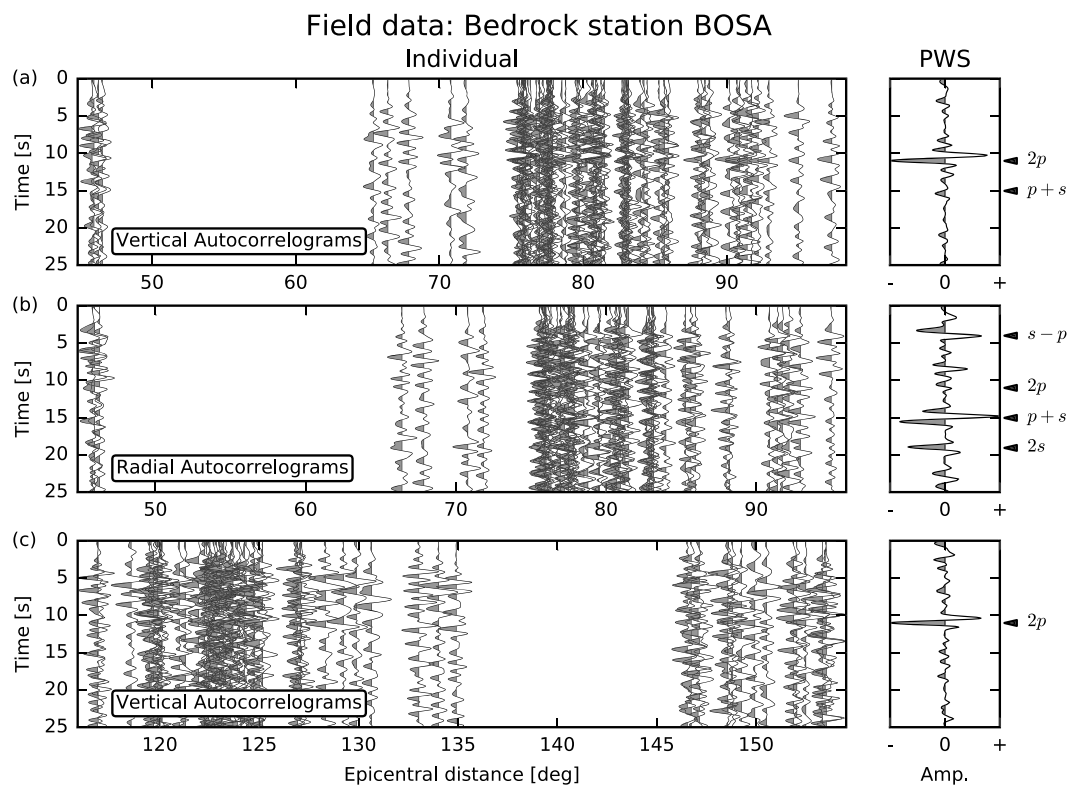


Figure 10. One-sided whitened autocorrelograms of field data recorded at the bedrock station BOSA; see Figure 3b for the geographical distribution of the events. (a) Vertical and (b) radial autocorrelograms of the P wave teleseismic data set; (c) and vertical autocorrelograms of the global teleseismic data set. For the explanation of the (left panels) individual autocorrelograms and (right panels) stacked autocorrelograms, see the captions of Figure 2.

hypocentral depths but also the source surrounding. Therefore, if earthquakes used in the stack cover a wide diversity of depths and geological structures, the incoherent source-side signals will cancel destructively, and the coherent receiver-side signals will emerge from the noise. The source-side signals might be an issue only if one has a limited number of earthquakes that all concentrate to a specific region in such a way that similar source-side signals are probably coherent in most individual autocorrelograms. In our featured cases, most selected earthquakes originate from broad and complex subduction zones in Southern Pacific and South America. They tend to originate at much greater depths than the reflectors under consideration, so our recovered signals are void of potentially hidden source side signals.

The two examples presented in this study are from the regions that share a common feature of having a sharp discontinuity separating the basement with a relatively simple layer above. The configuration favors efficient reflections of downgoing energy to the interface and transmits most the bounced energy up to the free surface without being scattered at intermediate interfaces along its way. Indeed, it is a common requirement of recent studies that show a prominent body wave reflection signals on a station stack [e.g., Zhan et al., 2010; Tibuleac and von Seggern, 2012; Gorbatov et al., 2013]. Therefore, we expect a comparable success of our method at a range of stations having similar subsurface situations. On the other hand, less favorable conditions, for example with the presence of a gradational discontinuity [e.g., Kennett et al., 2015; Kennett, 2015] or a complex layer structure [e.g., Sun and Kennett, 2016], generally require additional independent information to assist the detection of the discontinuities.

7. Conclusions

The use of stacked autocorrelograms from distant events at individual stations provides an effective means of extracting both P and S wave reflectivity. Resolution of shallow discontinuities is enhanced by an effective whitening procedure. By choice of events, so that arriving signals travel steeply in the structure beneath a receiver, we promote the constructive interference of vertical reflection signals.

We use carefully designed synthetic experiments and field data to demonstrate the feasibility of our approach. Both vertical and radial autocorrelograms are exploited to provide complementary information on the subsurface structure. With sharp discontinuities, the reflection signals are clear and easy to interpret, but lesser features can also be discerned in the reflectivity traces.

In the case of a station sitting on an ice cap, even though the ice is relatively thin, we are able to successfully use the autocorrelation technique to mark the P wave reflection from the ice-bedrock interface with a strong impedance contrast. This suggests that the approach may help resolve issues with shallow, pronounced sediment layers that corrupt receiver functions with reverberations, yielding information on V_p and V_s from the radial autocorrelograms.

The angular dependence of the P wave reflectivity extracted from the whitened autocorrelograms has the potential for being used in migration methods, and thereby imaging more complex structures where dense station deployments are available.

References

- Anandakrishnan, S., and J. P. Winberry (2004), Antarctic subglacial sedimentary layer thickness from receiver function analysis, *Global Planet. Change*, 42(1–4), 167–176, doi:10.1016/j.gloplacha.2003.10.005.
- Bensen, G. D., M. H. Ritzwoller, M. P. Barmin, A. L. Levshin, F. Lin, M. P. Moschetti, N. M. Shapiro, and Y. Yang (2007), Processing seismic ambient noise data to obtain reliable broad-band surface wave dispersion measurements, *Geophys. J. Int.*, 169(3), 1239–1260, doi:10.1111/j.1365-246X.2007.03374.x.
- Chaput, J., R. C. Aster, A. Huerta, X. Sun, A. Lloyd, D. Wiens, A. Nyblade, S. Anandakrishnan, J. P. Winberry, and T. Wilson (2014), The crustal thickness of West Antarctica, *J. Geophys. Res. Solid Earth*, 119, 378–395, doi:10.1002/2013JB010642.
- Cho, T. (2011), Removing reverberation in ice sheets from receiver functions, *Seismol. Res. Lett.*, 82(2), 207–210, doi:10.1785/gssrl.82.2.207.
- Claerbout, J. (1968), Synthesis of a layered medium from its acoustic transmission response, *Geophysics*, 33(2), 264–269, doi:10.1190/1.1439927.
- Ekström, G., M. Nettles, and A. M. Dziewoński (2012), The global CMT project 2004–2010: Centroid-moment tensors for 13,017 earthquakes, *Phys. Earth Planet. In.*, 200–201, 1–9, doi:10.1016/j.pepi.2012.04.002.
- Frasier, C. W. (1970), Discrete time solution of plane p-sv waves in a plane layered medium, *Geophysics*, 35(2), 197–219, doi:10.1190/1.1440085.
- Fretwell, P., et al. (2013), Bedmap2: Improved ice bed, surface and thickness datasets for Antarctica, *The Cryosphere*, 7(1), 375–393, doi:10.5194/tc-7-375-2013.
- Gorbatov, A., E. Saygin, and B. L. N. Kennett (2013), Crustal properties from seismic station autocorrelograms, *Geophys. J. Int.*, 192(2), 861–870, doi:10.1093/gji/ggs064.

Acknowledgments

We thank Brian L.N. Kennett, Malcolm Sambridge, and Benoit Tauzin for their extensive discussions and comments in the process of producing the manuscript and improving its quality. T.S.P. acknowledges Mariangela Guidarelli's supervision at the initial stage of this work on ambient noise autocorrelation, which was submitted as his thesis for the Postgraduate Diploma Degree at the Abdus Salam ICTP. We thank Robert Nowack, Victor Tsai, and the Associate Editor Sebastian Chevrot for providing insightful comments that improved the presentation of the manuscript. The facilities of IRIS Data Services, and specifically the IRIS Data Management Center, were used for access to waveforms, related metadata, and/or derived products used in this study. IRIS Data Services are funded through the Seismological Facilities for the Advancement of Geoscience and EarthScope (SAGE) Proposal of the National Science Foundation under cooperative agreement EAR-1261681.

- Hansen, S. E., A. A. Nyblade, J. Julià, P. H. G. M. Dirks, and R. J. Durrheim (2009), Upper-mantle low-velocity zone structure beneath the Kaapvaal craton from S-wave receiver functions, *Geophys. J. Int.*, 178(2), 1021–1027, doi:10.1111/j.1365-246X.2009.04178.x.
- Hansen, S. E., A. A. Nyblade, D. S. Heeszel, D. A. Wiens, P. Shore, and M. Kanao (2010), Crustal structure of the Gamburtsev Mountains, East Antarctica, from S-wave receiver functions and Rayleigh wave phase velocities, *Earth Planet. Sci. Lett.*, 300(3–4), 395–401, doi:10.1016/j.epsl.2010.10.022.
- James, D. E., F. Niu, and J. Rokosky (2003), Crustal structure of the Kaapvaal craton and its significance for early crustal evolution, *Lithos*, 71(2–4), 413–429, doi:10.1016/j.lithos.2003.07.009.
- Kennett, B. L. N. (1983), *Seismic Wave Propagation in Stratified Media*, chap. 9, Cambridge Univ. Press, London.
- Kennett, B. L. N. (2015), Lithosphere–asthenosphere P-wave reflectivity across Australia, *Earth Planet. Sci. Lett.*, 431, 225–235, doi:10.1016/j.epsl.2015.09.039.
- Kennett, B. L. N., E. Saygin, and M. Salmon (2015), Stacking autocorrelograms to map Moho depth with high spatial resolution in south-eastern Australia, *Geophys. Res. Lett.*, 42, 7490–7497, doi:10.1002/2015GL065345.
- Kohnen, H. (1974), The temperature dependence of seismic waves in ice, *J. Glaciol.*, 13(67), 144–147.
- Langston, C. A. (1979), Structure under Mount Rainier, Washington, inferred from teleseismic body waves, *J. Geophys. Res.*, 84(B9), 4749–4762, doi:10.1029/JB084iB09p04749.
- Lin, F.-C., and V. C. Tsai (2013), Seismic interferometry with antipodal station pairs, *Geophys. Res. Lett.*, 40, 4609–4613, doi:10.1002/grl.50907.
- Niu, F., and D. E. James (2002), Fine structure of the lowermost crust beneath the Kaapvaal craton and its implications for crustal formation and evolution, *Earth Planet. Sci. Lett.*, 200(1–2), 121–130, doi:10.1016/S0012-821X(02)00584-8.
- Oren, C., and R. L. Nowack (2017), Seismic body-wave interferometry using noise auto-correlations for crustal structure, *Geophys. J. Int.*, 208(1), 321–332, doi:10.1093/gji/ggw394.
- Ramirez, C., A. Nyblade, S. E. Hansen, D. A. Wiens, S. Anandakrishnan, R. C. Aster, A. D. Huerta, P. Shore, and T. Wilson (2016), Crustal and upper-mantle structure beneath ice-covered regions in Antarctica from S-wave receiver functions and implications for heat flow, *Geophys. J. Int.*, 204(3), 1636–1648, doi:10.1093/gji/ggv542.
- Randall, G. E. (1989), Efficient calculation of differential seismograms for lithospheric receiver functions, *Geophys. J. Int.*, 99(3), 469–481, doi:10.1111/j.1365-246X.1989.tb02033.x.
- Rondenay, S. (2009), Upper mantle imaging with Array recordings of converted and scattered Teleseismic waves, *Surv. Geophys.*, 30(4–5), 377–405, doi:10.1007/s10712-009-9071-5.
- Ruigrok, E., and K. Wapenaar (2012), Global-phase seismic interferometry unveils P-wave reflectivity below the Himalayas and Tibet, *Geophys. Res. Lett.*, 39, L11303, doi:10.1029/2012GL051672.
- Schimmel, M., and H. Paulssen (1997), Noise reduction and detection of weak, coherent signals through phase-weighted stacks, *Geophys. J. Int.*, 130(2), 497–505, doi:10.1111/j.1365-246X.1997.tb05664.x.
- Sun, W., and B. L. N. Kennett (2016), Receiver structure from teleseisms: Autocorrelation and cross correlation, *Geophys. Res. Lett.*, 43, 6234–6242, doi:10.1002/2016GL069564.
- Taylor, G., S. Rost, and G. Houseman (2016), Crustal imaging across the North Anatolian Fault Zone from the autocorrelation of ambient seismic noise, *Geophys. Res. Lett.*, 43, 2502–2509, doi:10.1002/2016GL067715.
- Tibuleac, I. M., and D. von Seggern (2012), Crust–mantle boundary reflectors in Nevada from ambient seismic noise autocorrelations, *Geophys. J. Int.*, 189(1), 493–500, doi:10.1111/j.1365-246X.2011.05336.x.
- Tkalčić, H., Y. Chen, R. Liu, H. Zhibin, L. Sun, and W. Chan (2011), Multistep modelling of teleseismic receiver functions combined with constraints from seismic tomography: Crustal structure beneath southeast China, *Geophys. J. Int.*, 187(1), 303–326, doi:10.1111/j.1365-246X.2011.05132.x.
- Vinnik, L. P. (1977), Detection of waves converted from P to SV in the mantle, *Phys. Earth Planet. In.*, 15(1), 39–45, doi:10.1016/0031-9201(77)90008-5.
- Wittlinger, G., and V. Farra (2012), Observation of low shear wave velocity at the base of the polar ice sheets: Evidence for enhanced anisotropy, *Geophys. J. Int.*, 190(1), 391–405, doi:10.1111/j.1365-246X.2012.05474.x.
- Zhan, Z., S. Ni, D. V. Helmberger, and R. W. Clayton (2010), Retrieval of Moho-reflected shear wave arrivals from ambient seismic noise, *Geophys. J. Int.*, 182(1), 408–420, doi:10.1111/j.1365-246X.2010.04625.x.
- Zhan, Z., V. C. Tsai, J. M. Jackson, and D. Helmberger (2014), Ambient noise correlation on the Amery Ice Shelf, East Antarctica, *Geophys. J. Int.*, 196(3), 1796–1802, doi:10.1093/gji/ggt488.
- Zhu, L., and H. Kanamori (2000), Moho depth variation in southern California from teleseismic receiver functions, *J. Geophys. Res.*, 105(B2), 2969–2980, doi:10.1029/1999JB900322.